ORIGINAL ARTICLE

Drilling performance of small holes on C$_f$/SiC composites with brazed diamond grinding rods

Kai Wang[1] · Qiaoru Sun[1] · Haotian Yang[2] · Xingjian Jiao[1] · Xinyong Wang[1] · Junping Li[1] · Liang Xu[1] · Guolong Zhao[2]

Abstract

Carbon fiber reinforced silicon carbide matrix composites (C$_f$/SiC composites) are lightweight, high strength, wear-resistant, and heat-resistant, making them widely used in aerospace and other industries. However, machining holes in C$_f$/SiC composites is a great challenge due to the anisotropy and high hardness of the material. In this paper, a brazed diamond grinding rod was employed to grind 1 mm diameter holes in C$_f$/SiC composites, and the influence of grinding parameters on grinding force, hole entrance/exit defects, and hole wall quality was investigated. In addition, the material removal mechanism of C$_f$/SiC composites and the wear mechanism of the diamond grinding rod were explored. The findings showed that the damage at the hole entrance and exit predominantly manifests as tearing and burring. The damage factor at the hole exit is 3.5% larger than that at the hole entrance, and the damage factor at both the hole entrance and exit reduces with the growth of spindle speed and the decrease of feed rate. In addition, the diameter errors of the hole entrances and exits are all less than 10%, and the entrance diameter is 2.9% larger than the exit. The hole wall defects include fiber fracture, silicon carbide matrix peeling, and inherent porosity, with poorer surface quality at fiber orientation angles (FOA) of 90° to 180°. The main wear mechanisms were identified as abrasive wear and the spalling of abrasive grains.

Keywords C$_f$/SiC composites · Brazed diamond abrasive rods · Entrance/exit defects · Hole wall defects · Tool wear

1 Introduction

Carbon fiber-reinforced ceramic matrix composites (CFRC-MCs) represent a class of advanced materials that combine the high strength and stiffness of carbon fibers with the excellent thermal and chemical resistance of ceramic matrices [1, 2]. C$_f$/SiC composites find wide applications in aerospace thermal protection materials, thermal structure parts, brake discs for high-speed trains, optics, and other fields due to their high strength, high-temperature resistance, wear resistance, and so on [3, 4]. The equipment utilizing these materials operates in extreme environments, necessitating high precision and quality. Owing to the high hardness, anisotropy, and other difficult machining characteristics of these materials lead to severe tool wear and even breakage during hole machining on C$_f$/SiCs [5–7], presenting a significant challenge in machining high-quality C$_f$/SiCs.

Research on the machining structure of CMCs has included studies on hybrid machining techniques like ultrasonic machining [8, 9], and laser-assisted machining [10], alongside conventional techniques like drilling [11], milling [12, 13], and grinding [14, 15]. Yan et al. [16] investigated the behavior of C/SiCs under air and aqueous conditions with nanosecond laser ablation, finding that ablation was severe in an air environment. A water layer's presence during processing not only improved the quality but also prevented SiO$_2$ deposition on the surface and reduced heat accumulation. Jiao et al. [17] identified three different ablation zones: edge-oxidized, edge-removed, and center-removed, in nanosecond laser ablation of blind holes in 2.5-dimensional C$_f$/SiCs. Zhang et al. [18] employed abrasive water jets cutting holes in C$_f$/SiCs led to increased variation in hole diameter from inlet to outlet as the jet distance increased. Moreover, high jet velocity resulted in more noticeable delamination

✉ Guolong Zhao
  zhaogl@nuaa.edu.cn

[1] Science and Technology On Advanced Functional Composites Laboratory, Aerospace Research Institute of Materials and Processing Technology, Beijing 00076, China

[2] College of Mechanical and Electrical Engineering, Nanjing University of Aeronautics and Astronautics, Nanjing 210016, China

defects. Zheng et al. [19] proposed a novel technique for polishing C_f/SiCs using an ultrasonically vibrating femtosecond laser, where pulse energy density mostly caused characteristic features like fiber breaking, fiber pullout, banded craters, and voids. Ultrasonic vibration not only removed dirt and debris and reduced surface oxidation but also increased the residual compressive stress of carbon fibers. In conclusion, laser machining tends to ablate the C_f/SiCs, resulting in poor accuracy of the machined slots and holes [20]. Processing holes with abrasive water jets lead to poor delamination defects of the processed hole and the roundness at the hole's entrance and exit due to difficult control over pressure and flow rate [21]. Vibration-assisted drilling and laser-assisted drilling are less efficient and not suitable for practical production machining. Therefore, conventional processes such as drilling and grinding are more appropriate for micro-hole machining.

Many scholars have focused on the process of grinding and drilling C_f/SiCs. Yang et al. [22, 23] used a 500 μm diameter PCD drill for machining holes in C_f/SiCs, studying the drilling characteristics. They discovered that due to weak rigidity, the cutting edge deviated radially at the point where the chisel edge contacted the C_f/SiCs, significantly reducing hole quality. To examine the impact of tool wear on machined hole quality, Zhang et al. [24] drilled C_f/SiCs using a 10 mm diameter PCD drill. They discovered that as the drill experienced wear, the roughness of the hole wall initially increased before decreasing. Li et al. [25] performed drilling tests on 3D-C/C composites with sintered diamond abrasive rods, analyzing the machining damage and tool wear mechanisms. The primary defects identified were tearing and burring, with abrasive grain scraping, fracturing, and spalling being the main wear forms. Li et al. [26] conducted groove milling tests on 3D-C/C composites using super abrasive diamond grinding rods, examining the impact of fiber orientation angle on the material removal mechanism. Fiber breakage due to bending, compression, and extrusion was observed at fiber orientation angles of 0°, 90°, and higher than 90°, respectively. Chen et al. [27] comparatively analyzed the wear rate of abrasive grains and the surface quality of machined surfaces when grinding C_f/SiCs with ceramic-bonded, resin-bonded, and electroplated diamond wheels. They concluded that the best surface quality was achieved with electroplated diamond wheels, which had a low wear rate. In summary, wear and chipping of the cutting-edge during drilling significantly impact hole quality, while radial runout of a less rigid cutting edge affects hole accuracy [28]. Since brazed diamond grinding rods are multi-fluted, chipping of a single grain has minimal effect on hole wall quality. The simultaneous action of multiple abrasive grains during tool contact minimizes radial runout, making grinding more suitable for machining micro-small holes.

Regarding existing studies, few scholars have investigated small-hole machining on ceramic matrix composites, with almost no research focusing on the characteristics of machining small holes in these composites using brazed diamond grinding rods. Thus, exploring the wear mechanism of diamond grinding rods and the material removal mechanism when machining C_f/SiCs is necessary. In this paper, a brazed grinding rod was used to machine holes with a diameter of 1 mm on C_f/SiCs to study the characterization of the hole grinding process. The investigation covered the grinding force magnitude at different spindle speeds (n) and feed rates (f), the damage at the hole entrance and exit, and the surface quality of the hole wall under various process parameters. Finally, the study examined the grinding rod's wear mechanism and the material removal process.

2 Experimental details

2.1 C_f/SiC composites and grinding tool

The material examined in this study comprises 2D C_f/SiC composites, with dimensions of 10 mm in length, 10 mm in width, and 5 mm in height. These composites consist of two types of fiber bundles: warp and weft, depicted in Fig. 1(a) and 1(b). Table 1 presents the mechanical properties of the 2D-C_f/SiCs. Figure 1(c) and 1(d) illustrate the utilization of a brazed diamond grinding rod as the grinding tool. Figure 1(e) depicts the brazing bond, which employs BNi_2 brazing material. BNi_2 brazing material, predominantly composed of nickel, boron, and silicon, provides the grinding rod with good high-temperature strength, oxidation resistance, and corrosion resistance. The abrasive grains employed are artificial polycrystalline diamond (PCD) grains, ranging in size from 100 μm to 150 μm. As seen Fig. 1(c_2), single-crystal diamond grains were cuboctahedra, consisting of square {100} and triangular {111} faces, along with strong impact toughness and thermal stability. Notably, the {100} and {111} faces randomly contacted the C_f/SiC composites. The base material of the grinding rod is cemented carbide, with overall dimensions of 50 mm, featuring a cutter head portion measuring 20 mm in length and 1 mm in diameter.

2.2 Experimental setup and measurement

The study utilized a Ning Qing 3-axis CNC milling machine (shown in Fig. 2(a), with a maximum n of 20000 r/min. A single-factor experiment was conducted, with f) set at 1 μm/r, and n varied in increments of 2000 from 12000 r/min to 20000 r/min. While keeping a constant speed of 16000 r/min, f was adjusted in intervals of 0.25 from 0.75 μm/r to 1.5 μm/r. Additionally, the experiments used a peck drilling

Fig. 1 C$_f$/SiC composites and grinding tool: **a** the schematic diagram of 2D C$_f$/SiC composites, **b** surface morphology, **c** sidewall morphology of brazed diamond grinding rod, **d** top morphology of brazed diamond grinding rod and (**e**) Line EDS of grinding tool

Table 1 The mechanical properties of 2D-C$_f$/SiCs

Parameters	Value
Density (g/cm^3)	1.81
Fiber volume (%)	33.4
Surface porosity (%)	< 10
Shear strength (MPa)	75
Bending strength (MPa)	413
Compressive strength (MPa)	280
Fracture toughness (MPa·m$^{1/2}$)	13

method with a single feed depth of 0.1 mm. No cutting fluid was used during the hole grinding process on C$_f$/SiCs.

To measure the grinding force in real time, the C$_f$/SiC composites were mounted on a piezoelectric dynamometer. A Kistler 9256C1 piezoelectric dynamometer, along with a data collector, was used to capture the grinding force (Fig. 2(a)). The sensor's threshold sensitivity is less than 0.001 N. Surface roughness evaluation was performed using a Sensofar S Neox 3D laser confocal microscope. Additionally, the optical morphology of the grinding rods was examined using a KEYENCE VHX-6000 microscope.

3 Results and discussion

3.1 Grinding force

Grinding force is an important parameter for monitoring the grinding process and affects the wear of the grinding rod and the quality of the machined hole. In Fig. 3, measurements in three directions, namely F_x, F_y, and F_z, conducted during the experiment, are shown. The grinding process is divided into three stages: the feed stage, the stabilization stage, and the withdrawal stage. A sampling frequency of 10 kHz is employed throughout the experiment. Initially, the force signals from the dynamometer are inputted into the Dynoware program. Subsequently, signal drift is rectified by utilizing the software's drift adjustment feature. Thirdly,
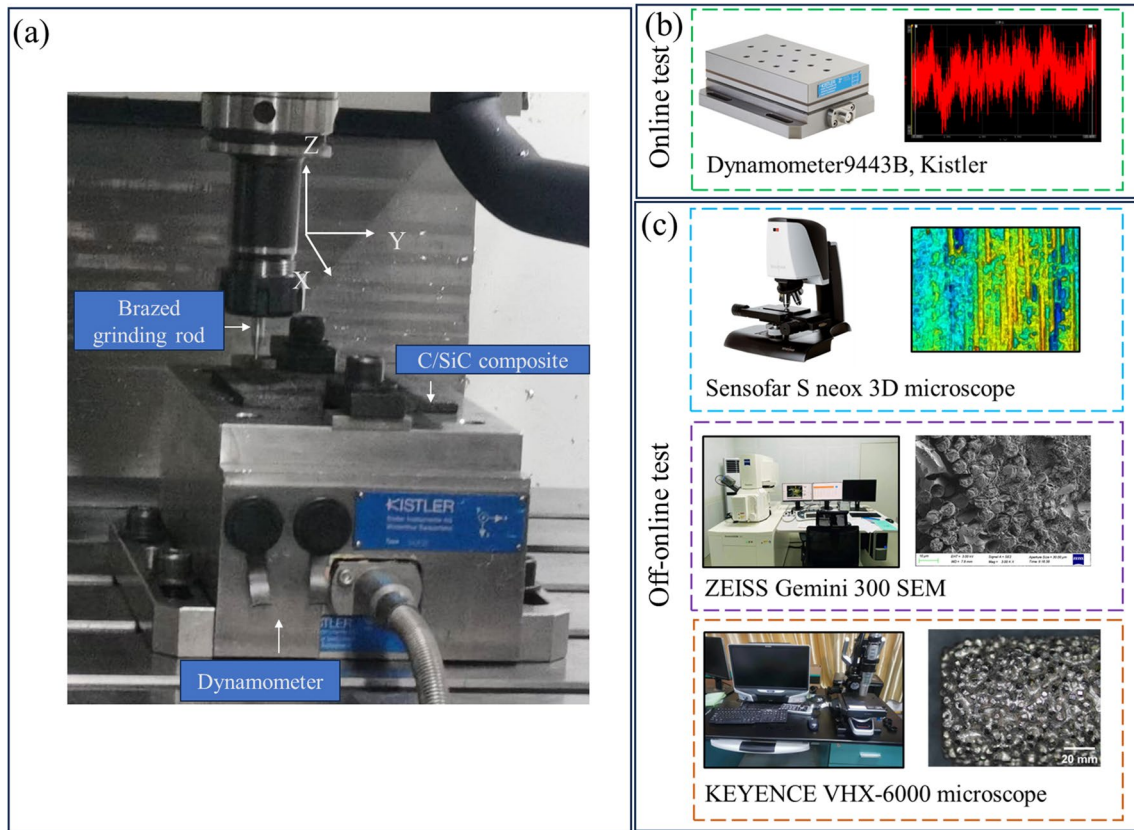
Fig. 2 **a** Setup of grinding on C$_f$/SiCs and (**b**) online test equipment and (**c**) off-online test
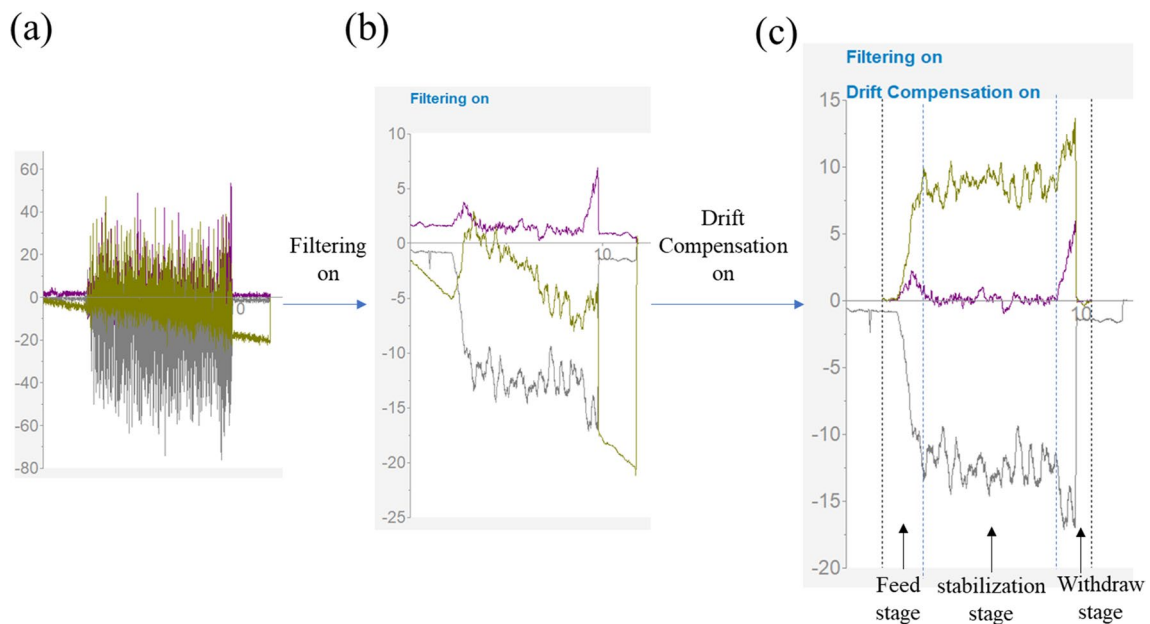

Fig. 3 The diagram of the (**a**) original grinding force signal, (**b**) filtered signal and (**c**) drift compensated signal

the program's 10 kHz low-pass filter capability is harnessed to filter the force signal. Low-pass filters are instrumental in generating smoother and slower signal shifts by removing high-frequency components and smoothing out signal

fluctuations. Finally, the Origin program is loaded with the intercepted force signals. Statistical data are then derived by tallying and averaging the peak cutting forces during the signals' stabilization period. Given that the Z direction serves as the main feeding direction, F_z during the grinding process substantially surpasses F_x and F_y. A multitude of abrasive grains exhibit non-uniform distribution on the surface of the grinding rod, with the cutting edge direction and angle of the abrasive grains varying across different positions. Furthermore, the fluctuation in grinding process force is exacerbated by the presence of pores on the surface of the C_f/SiCs.

The average grinding forces F_x, F_y and F_z under various n during the grinding process are shown in Fig. 4(a). The grinding force F_z demonstrates an initial increase followed by a subsequent decrease with the escalation of f. The thrust force F_z increases from 9.2 N to 17.3 N as n grows from 12000 to 18000 r/min. The squeezing effect between abrasive grains and C_f/SiCs corresponds to the increasing n. The higher reaction force causes an equal growth in both grinding temperature and grinding force. Conversely, F_z decreases from 17.3 N to 16.8 N as n grows from 18000 to 20000 r/min. On one hand, the decline in friction coefficient ensues from the heating of C_f/SiCs, ultimately leading to a reduction in grinding force. On the other hand, the escalation in grinding speed results in an increased chip cross-sectional area. This increment is offset by a reduction in actual cutting edges, resulting in diminished grinding forces. As f increases, both radial force and thrust force exhibit proportional increments (as depicted in Fig. 4(b)). This phenomenon is attributed to the escalating f, which leads to a rise in the material removal rate and the effort required to rise, driven by an elevated in both the frictional force and thermal energy. Consequently, the thermal energy is converted into cutting heat, leading to a rise in the temperature. On one hand, heightened f leads to excessive abrasive wear and boost impingement between the abrasive grains and C_f/SiCs, causing a growth in the formation. The amplified chips, in turn, lead to a corresponding rise in frictional force, which raises the grinding force. On the other hand, heightened reaction forces enhance the squeezing and scoring effect of individual abrasive grains as f increases.

3.2 Surface quality of hole entrances and exits

The quality of the hole entrance and exit significantly influences the assembly performance. Thus, the forms of damage at the hole entrance and exit were studied, the damage assessment criteria were established, and the influence of the process parameters on the morphology of these entrances and exits was explored. In C_f/SiCs, delamination is relatively uncommon due to the strong support from the SiC matrix. Therefore, the study primarily focuses on tearing and burring defects. Figure 5(a) illustrates that tearing occurs when the grinding rod applies significant pressure on the final layer of C_f/SiCs during the drilling out stage, causing the carbon fibers to separate axially from the SiC and break. This separation leads to tearing defects. According to Fig. 5(b), some separated but intact carbon fibers spring back in the absence of grinding forces, forming a burr at the hole exit. Moreover, Fig. 5(c) indicates that spalling of the SiC matrix due to excessive radial forces and radial runout at the neck of the grinding rod results in edge-breaking defects.

Figure 6 demonstrates the morphologies of the hole exit and entrance under various feed rates (f) and spindle speeds (n). Figure 6(b) shows significant edge chipping at an f of 1.5 μm/r. This is attributed to increased radial runout of the tool at higher f and the resultant high radial force leading to chipping defects. Figure 6(c) shows that a lower f of 0.5 μm/r results in high surface quality at the hole exit. Figure 6(d) indicates considerable ripping flaws at the hole exit with an f of 1.5 μm/r. Figures 6(e) to 6(h) present the morphologies of the hole entrance and exit across different n values. Figures 6(e) and 6(f) show that significant burrs are present at the hole exit at a spindle speed of 12000 r/min, due to fewer dynamic abrasive particles and a lesser cutting effect at lower n, hindering effective carbon fiber removal.

Fig. 4 **a** The grinding force under various spindle speeds and (**b**) The grinding force under various feed rates
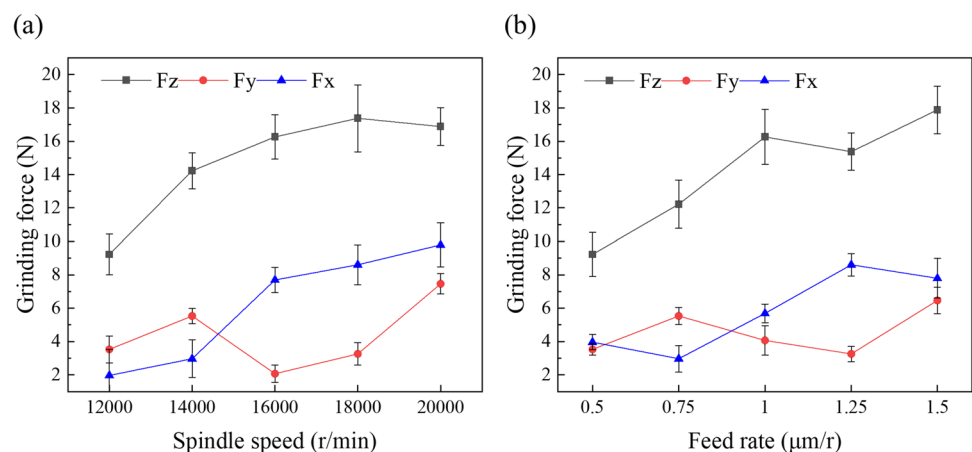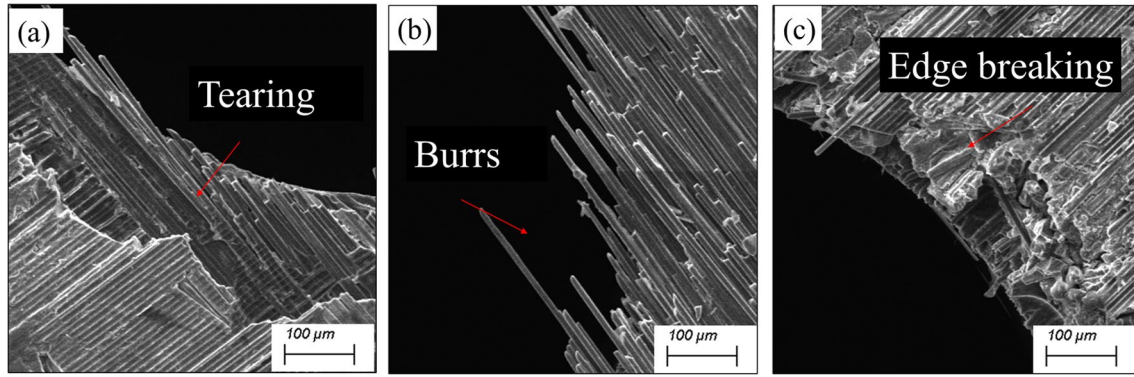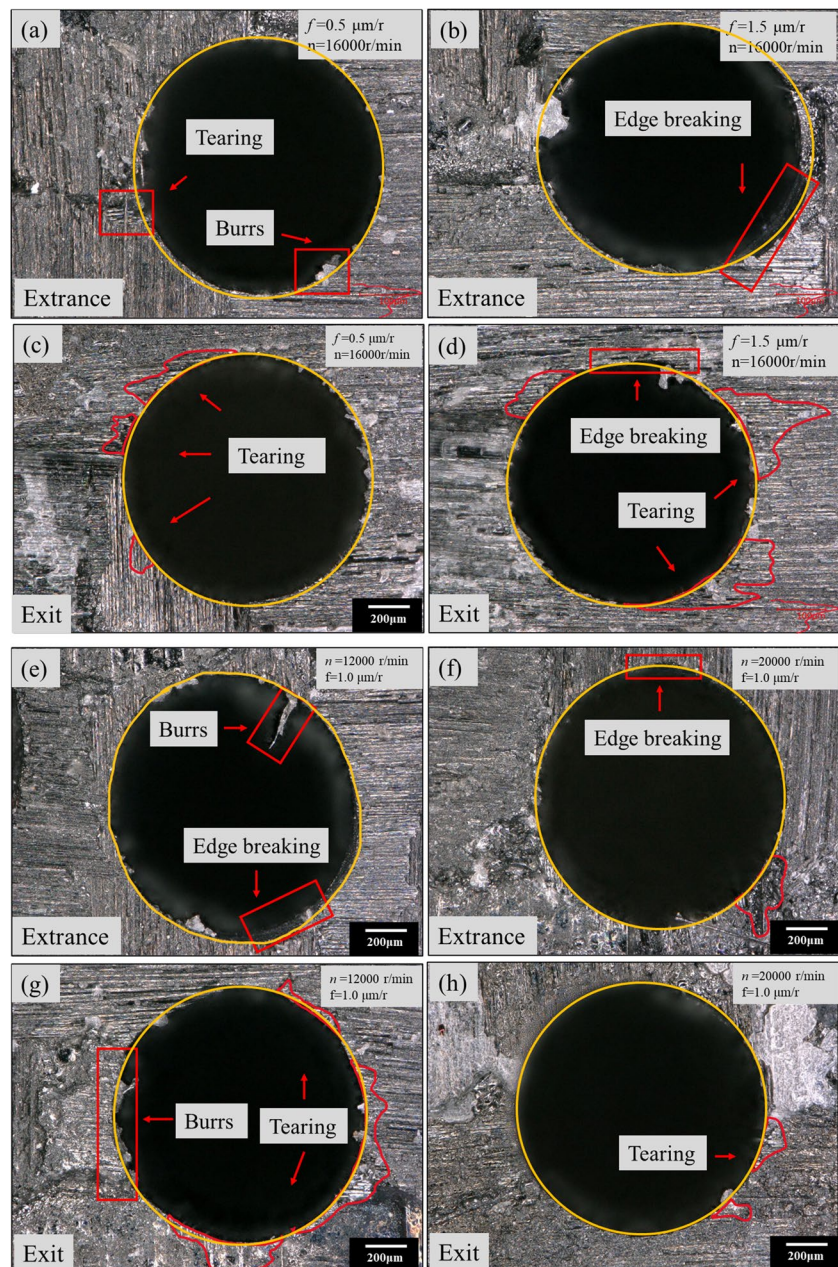
Fig. 5 Defects of hole entrance and exit

Fig. 6 The entrance and exit morphologies of holes at different feed rates and spindle speeds

An analysis of the entrance and exit morphologies indicates poor roundness at the hole entrances, primarily because of varying exposure heights of abrasive granules at the end of the grinding tool, which leads to radial slipping of the grinding tool. Furthermore, the hole exit exhibits more defects. During the grinding-in stage, the SiC matrix supports the surface layer of the material, preventing it from deforming downward. However, in the grinding-out stage, this layer receives weak support and undergoes significant deformation downward, leading to pronounced burr and tear defects.

To visualize the damage at the hole entrance and exit, the surfaces were analyzed using the Keens VHX-6000 high-resolution microscope. Figure 7(b) shows the identification of tear and burr defects on the surfaces of the hole entrance and exit using the microscope's 3D contour recognition function. Figure 7(c) introduces the method for quantifying the degree of tear and burr defects through a damage factor (F_d), calculated as per Eq. (1).
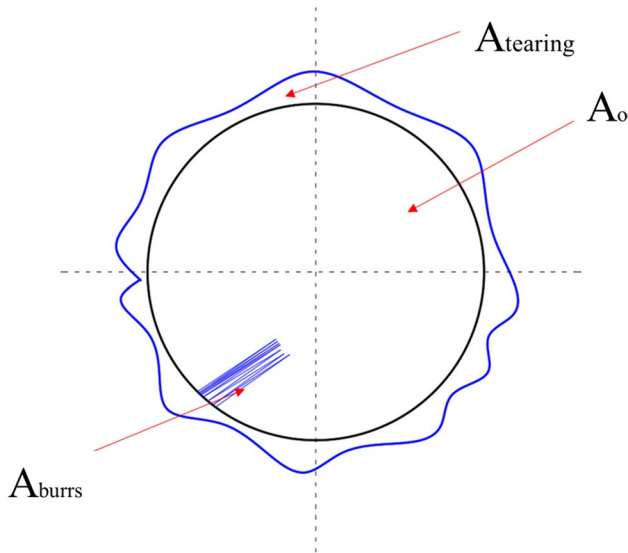
$$F_d = \frac{A_t + A_b + A_o}{A_o} \tag{1}$$

where A_t represents the area of tearing, A_b denotes the area of burrs, and A_o denotes the area of the machined hole.

Figure 8 shows that the damage factor at the hole exit exceeds that at the hole entrance. This discrepancy arises because the lower layer of material provides stronger support to the top layer during grinding, resulting in lesser tearing and burring at the hole entrance. As illustrated in Fig. 8(a), the damage factor for both the hole entrance and exit decreases with an increase in n. Conversely, Fig. 8(b) shows that the damage factor increases as f is reduced. The reduction in the squeezing impact of the abrasive grains on the final layer of Cf/SiCs with lower n and f values leads to a decrease in tearing and burring defects, explaining the reduction in F_z.

The diameter error for both the hole entrance and exit remains below 10%. Figure 9(a) demonstrates that the inlet diameters of the holes exceed 1000 μm, while those at the exit are less than but close to 1000 μm. This variation is attributed to the differing mechanical properties of the materials being cut, influenced by the anisotropic properties of C_f/SiCs. This condition causes the grinding rod to deflect, resulting in a maximum diameter (D_{max}) of the entrance holes exceeding 1000 μm. Additionally, accuracy issues with the holder and spindle vibration at high n values lead to radial runout of the tool, further explaining why the entrance diameter is larger than 1000 μm. On the one hand, some of the carbon fibers of the abrasive grains are not completely severed when cutting the final layer of C_f/SiCs, so the diameter hole exit is partially smaller than 1000 μm. On the other hand, wear on the abrasive grains reduces the exposed grain height as grinding progresses, leading to a decrease in D_{max} at the exit. Tearing contributes to an irregular hole shape, marginally increasing the exit's D_{max} above 1000 μm. Increased grinding depth provides support to the grinding rod from the hole wall, mitigating the flexural deformation

Fig. 7 Schematic diagram of hole entrance/exit damage factor

Fig. 8 The damage factor at different (**a**) spindle speeds and (**b**) feed rates
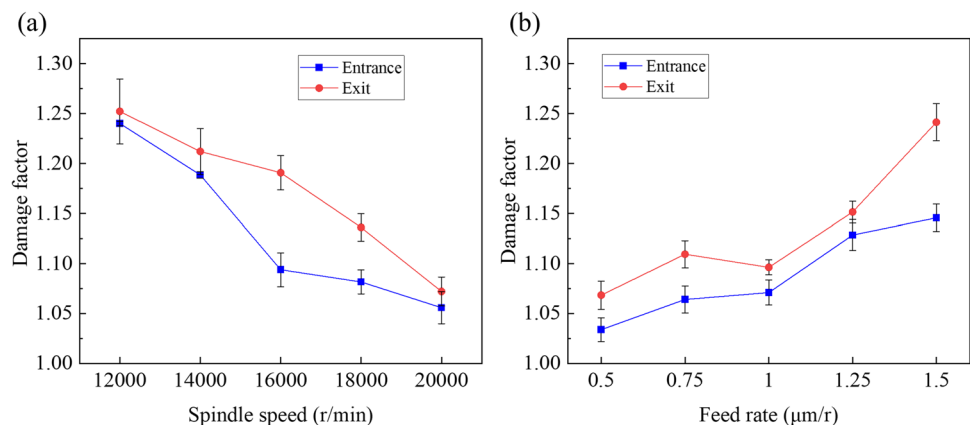
Fig. 9 The diameter of the hole exit and entrance under various (**a**) test groups, (**b**) spindle speeds and (**c**) feed rates

3.3 Surface quality of hole wall

One of the most crucial factors in determining the suitability of a hole is its surface quality. Imperfections in the hole wall will compromise the component's durability and structural integrity. Cracks and burrs on the hole wall serve as defects that might lead to the component's rupture or failure during operation. Therefore, examining the quality of the hole wall is critical.

The hole wall of C_f/SiCs cannot reach the smoothness of the metal materials, attributed to the significant differences in mechanical properties between carbon fiber and the SiC matrix. The C_f/SiCs, prior to machining, exhibit inherent defects such as pores. As shown in Fig. 10, the grinding process introduces new machining defects on the hole wall. The primary damage forms in carbon fiber include fiber pull-out, fiber fracture, and interface debonding, whereas the SiC matrix primarily exhibits brittle fracture. Due to the

of the grinding rod and thus, the D_{max} at the hole exit is closer to 1000 µm. As displayed in Fig. 9(b) and 9(c), neither n nor f has a linear effect on the diameter of the hole exit. However, with increasing f, the D_{max} at the hole entrance tends to rise, yet n does not linearly affect the D_{max} at the entrance.

differing mechanical properties of carbon fibers and SiC, their removal processes differ. SiC's relatively low fracture toughness leads to immediate crack propagation and brittle fracture under stress. In contrast, carbon fiber, known for its excellent tensile, flexural, and compressive strength, breaks only after undergoing a certain degree of deformation, not instantly under compressive, shear, or bending stresses. As a result, fiber pull-out and debonding occur. In addition, carbon fibers and the SiC matrix fracture to varying degrees when subjected to stresses exceeding their strength. The grinding hole acts as a confined space, leading to heat accumulation within the hole walls. During the grinding rod's operation, chips are discharged through the gaps between the abrasive grains, rendering the chip removal capacity of the grinding rod poor compared to that of a drill. As the abrasive grains wear, the grinding temperature rises and the chip removal space diminishes, causing chips to adhere to the C_f/SiCs surface of the grinding tool.

The 3D morphology of the hole wall is shown in Fig. 11, where the damaged forms of carbon fiber and SiC can be distinguished based on the contour curve of the hole wall. The protrusion, identified as a chip sticking spot, is highlighted in the contour curve A of Fig. 11(c). The depression, indicating a fiber pull-out defect, is shown in curve B of Fig. 11(d). Similarly, the area where the contour curve C
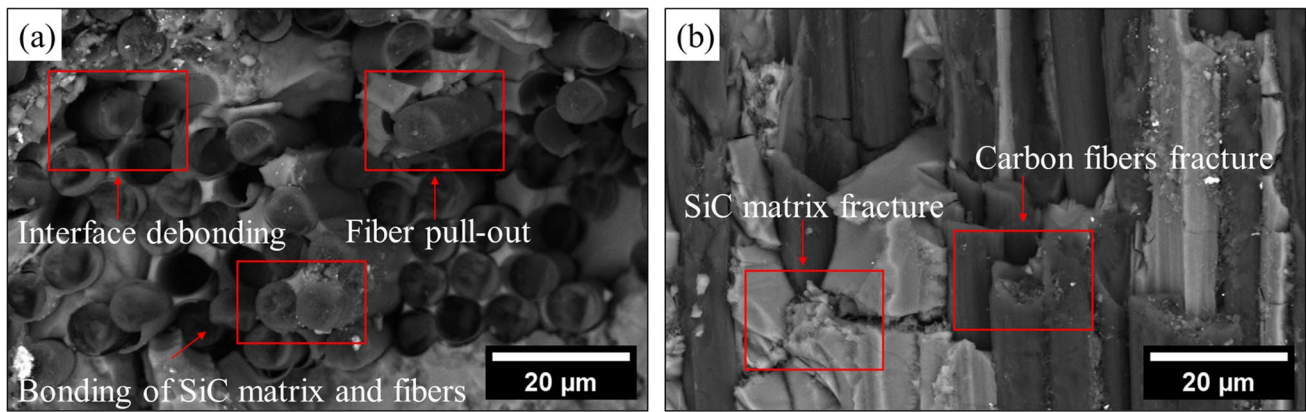
Fig. 10 The defects of C_f/SiCs machined surface: **a** Interface debonding, fibers pull-out, bonding of SiC matrix and fibers, and **b** SiC matrix fracture and carbon fiber fracture
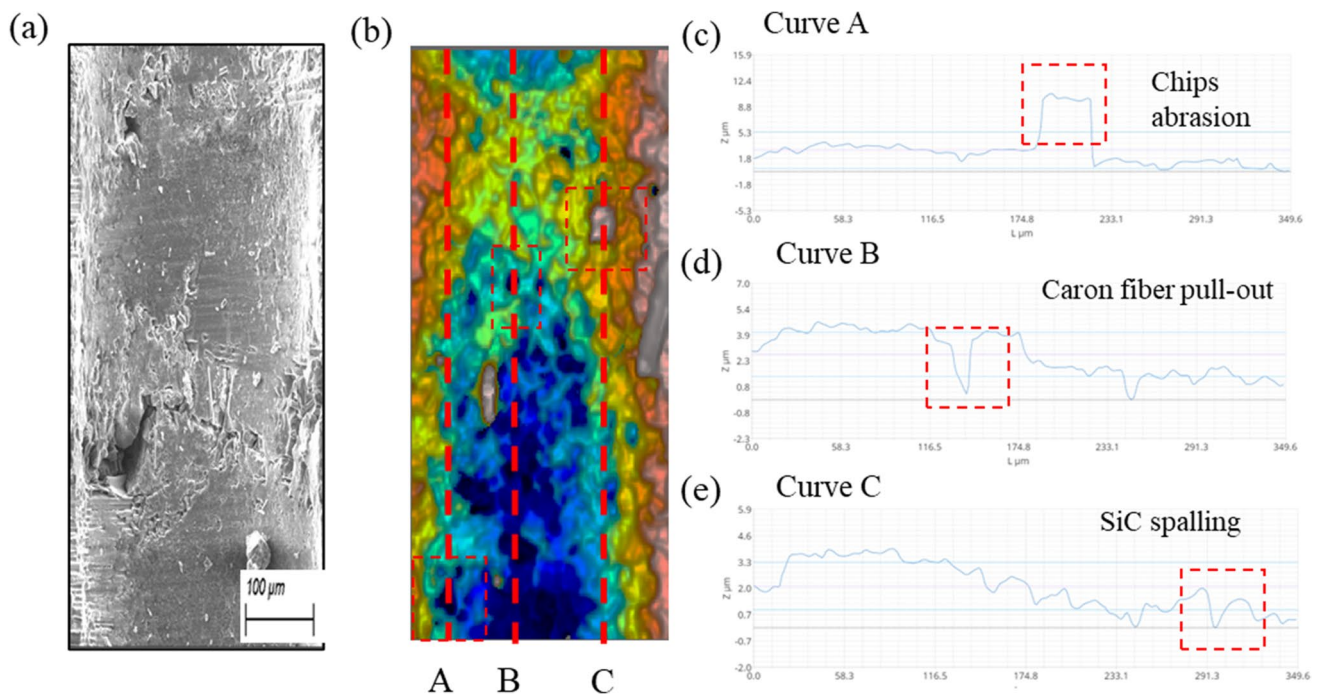

Fig. 11 The (**a**) SEM image, (**b**) 3D morphology of the hole wall, and (**c–e**) contour curves of A-C in Fig. 11(b) respectively

drops repeatedly in Fig. 11(e) marks the SiC matrix spalling defect.

The surface quality of the hole wall is closely related to the process parameters. Figure 12(a) shows the morphology of the hole wall at a n of 12,000 r/min, where the fibers undergo macroscopic brittle fracture with a deep fracture, resulting in a poor surface quality, along with pits formed by a large amount of exfoliation of the SiC matrix. In Fig. 12(c), at a rotation speed of 20,000 r/min, extensive exfoliation of the SiC matrix, forming pits, was not observed, resulting in improved surface quality. Figure 12(g) shows that S_a of the hole wall decreases from

6.673 µm to 4.332 µm as n increases. This improvement is attributed to the increased interaction between abrasive grains and the hole wall per unit time, which truncates the crack propagation on the hole surface, thereby transitioning the macroscopic brittle fracture of fibers to microscopic brittle fracture. As the n increases, the grinding force gradually decreases, resulting in less brittle fracture and better hole wall quality. The surface morphology at a f of 0.5 µm/r, depicted in Fig. 12(d), small pits were observed as well as tearing of carbon fiber bundles. Figure 12(e) illustrates the hole wall morphology at a f of 1.0 µm/r, where minimal chip adhesion and predominantly
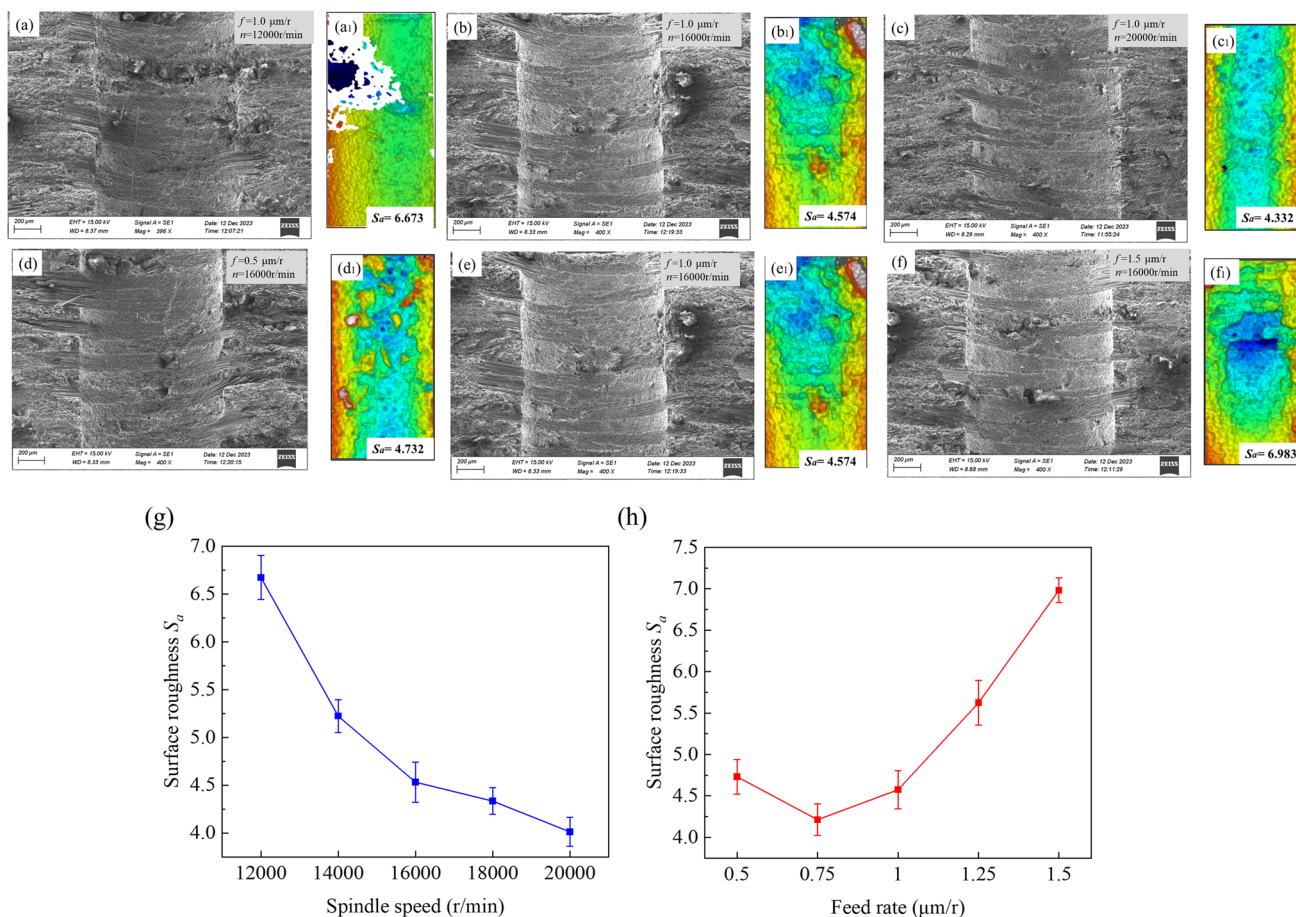
Fig. 12 **a**-f The surface morphology and 2D topographies of the hole wall at different spindle speeds and feed rates; The S_a of the hole wall at different (**g**) spindle speeds and (**h**) feed rates

small brittle fractures in the fiber contribute to good surface quality. The morphology at f of 1.5 µm/r, shown in Fig. 12(f), shows that large fiber tears and SiC spalling at the edges, deteriorating the surface quality. According to Fig. 12(h), as the f increases from 0.5 µm/r to 1.0 µm/r, the S_a decreases from 4.732 µm to 4.574 µm. However, increasing the f from 1.0 µm/r to 1.5 µm/r raises the S_a from 4.574 µm to 6.983 µm. At lower f, the quantity of effective dynamic grits is insufficient, compromising the hole wall quality. Enhancing the f increases the number of effective dynamic grains, the force and stress per unit area of the material is more uniform. Therefore, no pit defects due to SiC matrix spalling and carbon fiber bundle pull-out occur, improving the surface quality. In addition, the increase in the number of effective dynamic grains avoids the falling off of single abrasive grains due to high stress, which increases the cutting performance of the tool and contributes to the improvement of surface quality. However, the F_z gradually grows as the f continues to increase, and the chance of cracks in the hole wall increases during machining, resulting in higher S_a.

3.4 Material removal mechanisms

There is a significant difference in the morphology of C_f/SiCs when fiber orientation angles (FOA) vary, attributed to the large disparity in mechanical characteristics of carbon fibers with different orientations. The schematic diagram of fiber orientation angles is shown in Fig. 13(a). The morphology of the hole wall at FOA = 0° is shown in Fig. 13(b), where interlayer separation between carbon fibers and the SiC matrix occurs, and the surface is smooth at locations of fiber debonding. However, the surface quality at locations of fiber fracture is poor due to the unpredictable nature of fracture locations. Figures 13(c) depict the appearance of the hole wall when FOA is 45°, with only a minor area of brittle removal of the SiC matrix observed. The carbon fiber roots remain encased in the SiC matrix, which provides better support for the fibers. Figures 13(d) depict the appearance of the hole wall when FOA is 90°, uneven distribution of fiber fracture depth observed. The carbon fiber fracture, occurring near the cutting edge of the abrasive grains, leads to a more consistent fracture depth and, as a result, a high-quality

Fig. 13 The micro-morphology of C_f/SiC composites machined surface under different FOAs
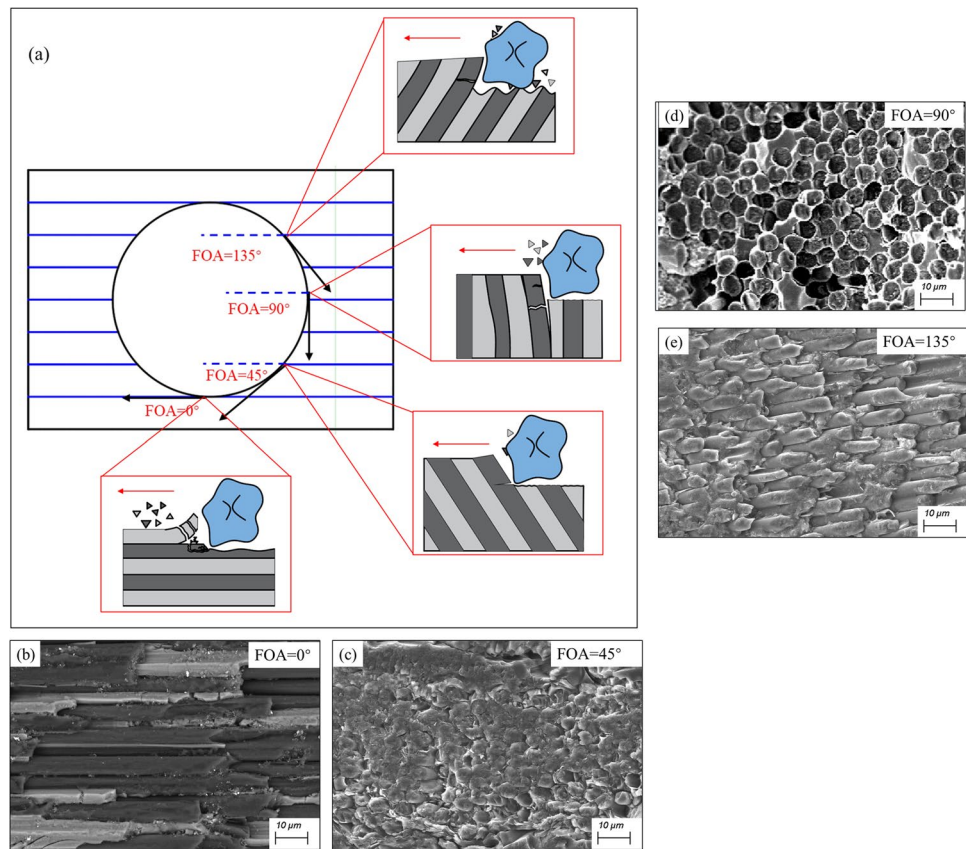
hole wall. The morphology of the hole wall, when FOA is 135°, is shown in Fig. 13(e), where the SiC undergoes brittle removal over a larger area, and the fibers are almost exposed on the surface of the hole wall, resulting in poor SiC support for the fibers. Primarily, carbon fiber cracks due to bending force, and the deeper fracture position leads to poor surface quality. In addition, there is less space for chip removal at FOA = 90–180° than at FOA = 0–90°, causing heat to accumulate from the generated chips, which intensifies the wear of the abrasive grains. The undischarged chips continuously scrape the machined surface, potentially leading to fracture of the interface layer, making carbon fiber debonding more pronounced at FOA values ranging from 90 to 180°.

The morphologies of C_f/SiCs chips are shown in Fig. 14. Carbon fiber chips are in the form of long strips and SiC chips are block-shaped. Process parameters significantly influence chip morphologies. The chip morphology at a large f is shown in Fig. 14(a), where long carbon fiber chips and larger SiC chips are observed. The chip morphology at small f is shown in Fig. 14(b), displaying short carbon fiber chips and fine SiC chips. A low n and high f resulted in the cutting edge removing more C_f/SiCs per unit time, increasing chip thickness and, consequently, a larger volume of SiC chips and longer carbon fibers. The removal of a large volume of the SiC matrix causes carbon fiber debonding, resulting in carbon fiber bundle chips. Conversely, higher n

and lower f result in the cutting edge removing less C_f/SiCs per unit time, decreasing chip thickness, thus shorter carbon fiber chips and a smaller volume of SiC chips are observed, with almost no carbon fiber bundle chips evident.

3.5 Tool wear mechanisms

During the grinding process, the rebound of the fibers and the friction of the SiC matrix leads to the wear of abrasive grains. This study conducted wear tests on brazed diamond grinding rods at n of 20000 r/min and f of 1.5 µm/r.

The wear morphology of the grinding rods was examined after grinding 2, 4, and 6 holes. Due to the significant impact of C_f/SiCs, stress and cutting heat concentrate nearly entirely on the cutting edge. The abrasive grains tend to produce small cracks and even minor breakage after grinding 2 holes, as demonstrated in Fig. 15(a) and 15(d). After grinding 4 holes, the abrasive grains experience serious scraping, yet catastrophic failure does not occur, as demonstrated in Fig. 15(b) and 15(e). The wear surface of the abrasive grains continues to expand, and the incidence of chipped edges among the grains increases. At this stage, chipping of the cutting edge and abrasive wear become the main mechanisms of wear. After grinding 6 holes, mechanical and thermal stress accumulate significantly, leading to serious chipping of the cutting edge of diamond grains,
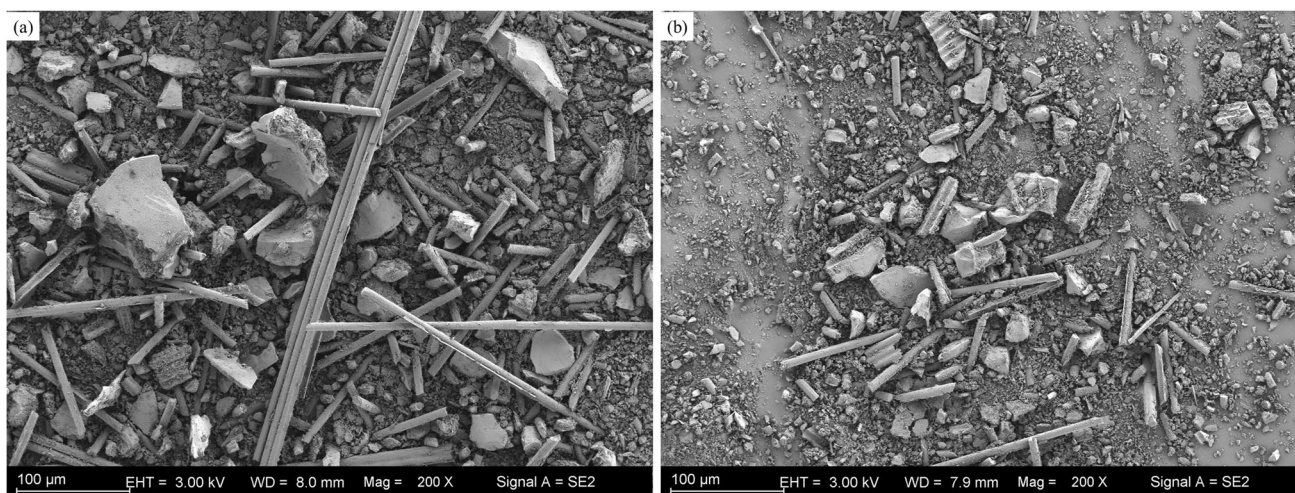
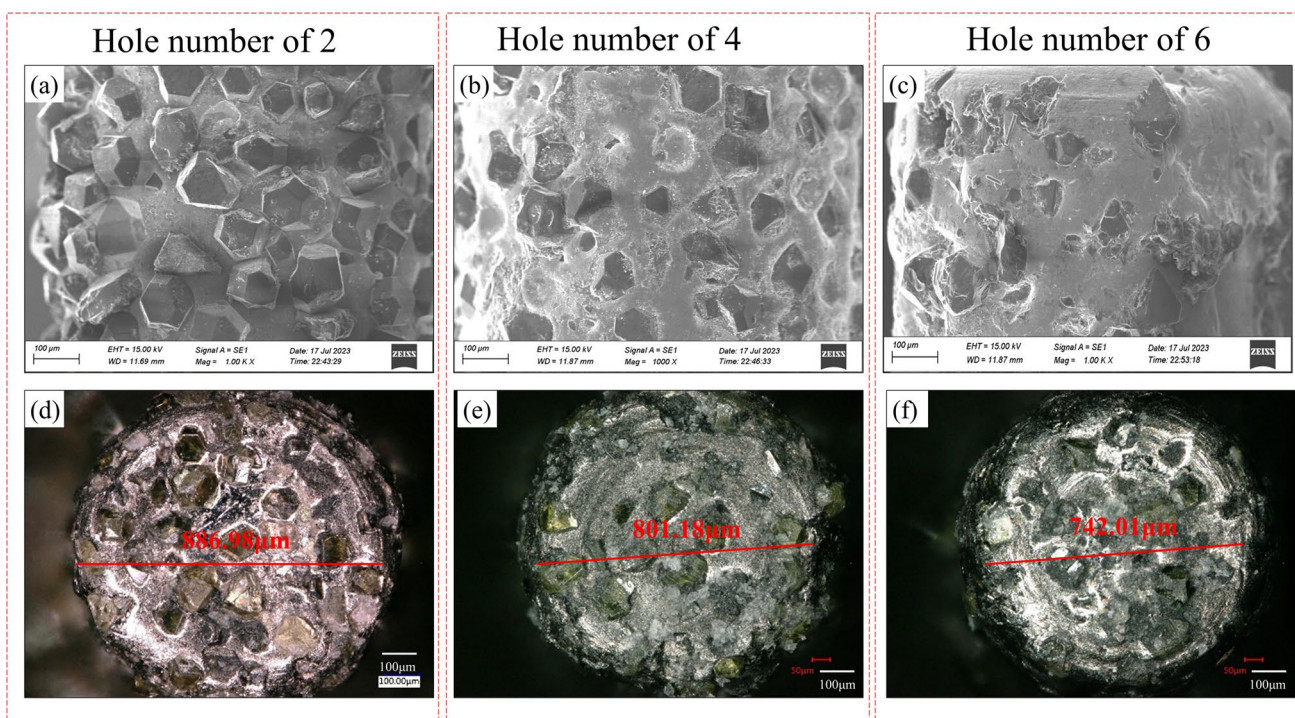**Fig. 14** The morphology of carbon fiber chips and SiC chips

Fig. 15 Morphologies of the worn surface of diamond abrasive rods when the grinded hole number is (**a**) 2, (**b**) 4, and (**c**) 6

as demonstrated in Fig. 15(c) and 15(f). The grinding rod becomes severely blunted, and the chipping further reduces the sharpness of the diamond grains. As a result, an abrasive grain breakout was detected. In addition, the spalling of abrasive grains emerges as the primary wear mechanism due to the impact of C_f/SiCs and severe abrasive wear after grinding 6 holes. The diameters of the grinding tools are 886.98 μm, 801.18 μm, and 742.01 μm after machining 2, 4, and 6 holes, respectively.

The elemental distribution on the surface of the grinding tool, when grinding 2, 4, and 6 holes, is illustrated in Fig. 16. The mapping EDS results are shown in Fig. 16(a), 16(b), and 16(c). The content of elemental Ni was 20.35%, 25.50%, and 31.13% for 2, 4, and 6 ground holes, respectively. Similarly, the content of elemental C was 75.44%, 63.14%, and 55.22% for 2, 4, and 6 ground holes, respectively. This trend indicates that as the number of holes increases, the diamond grits wear and flake off, exposing
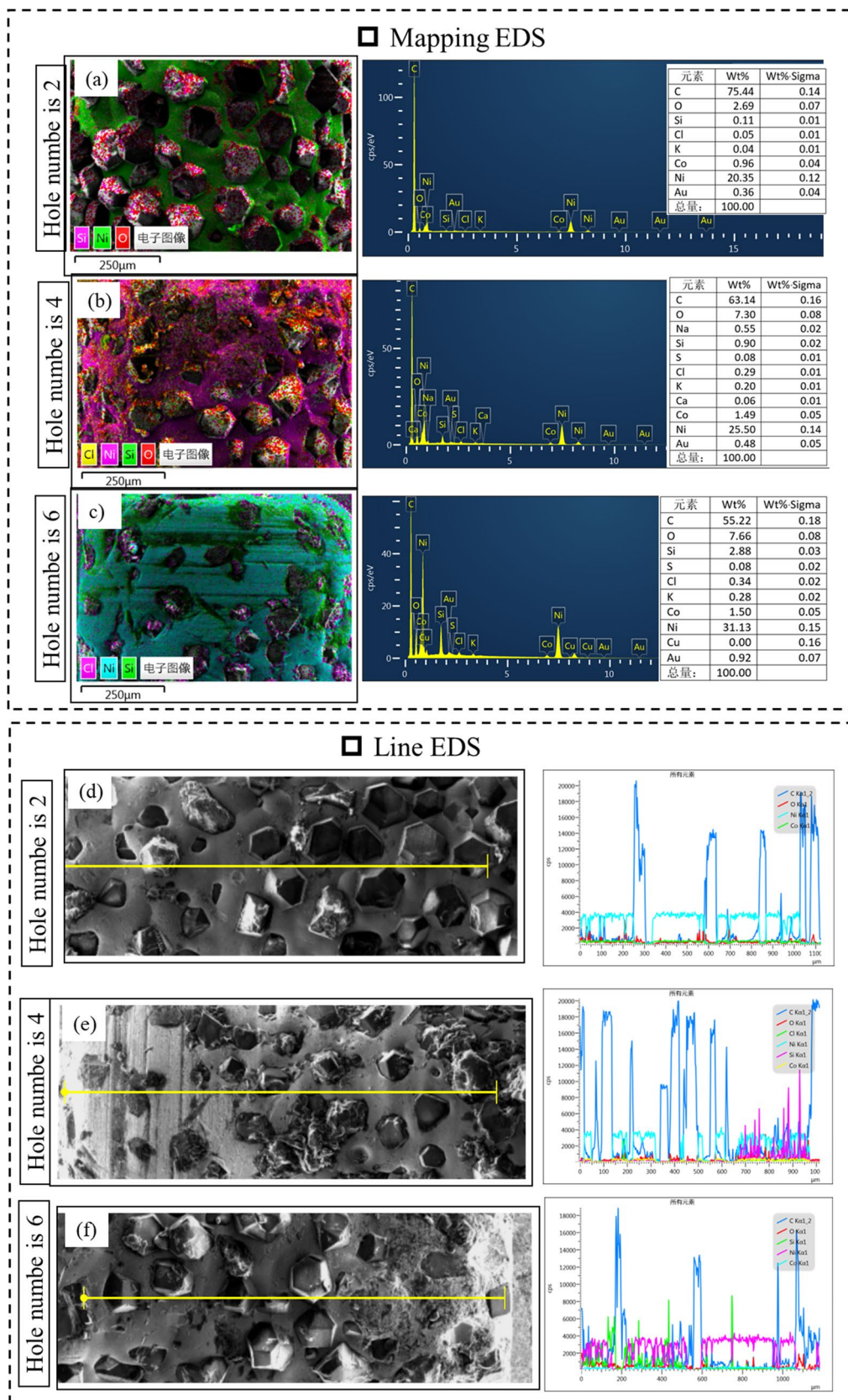
Fig. 16 The elemental distribution on the surface of the grinding tool when the number of grinding holes is 2, 4 and 6:**a**, **b** and **c** The mapping EDS of the grinding tool; **d**, **e** and **f** The line EDS of the grinding tool

more of the brazing material and cemented carbide matrix, leading to a decrease in C content and an increase in Ni content on the surface. Additionally, tool wear is associated with a gradual increase in the amount of Si element on the surface, caused by SiC chips adhering to the tool surface. The line EDS results, shown in Fig. 16(d), 16(e), and 16(f), reveal higher contents of Ni and Si elements near the top region of the grinding tool, where the C content is lower. The main reason is that abrasive grains near the top undertake the bulk of grinding work, experiencing

higher temperatures and forces, leading to severe wear and more chip adhesion.

The wear morphologies of abrasive grains under different f and n are shown in Fig. 17. As f decreases, the abrasive grains experience significant wear. For example, the wear level is higher in Fig. 17(a) than in Fig. 17(b), and higher in Fig. 17(e) than in Fig. 17(f). This occurs because the contact time between the abrasive grains and the C_f/SiCs per unit of time increases as f decreases, causing more wear on the abrasive grains. Similarly, as n increases, the abrasive

Fig. 17 Wear morphology of abrasive grains on (**a-d**) the side and (**e-h**) the end of brazed grinding rod at different feed rates and spindle speeds
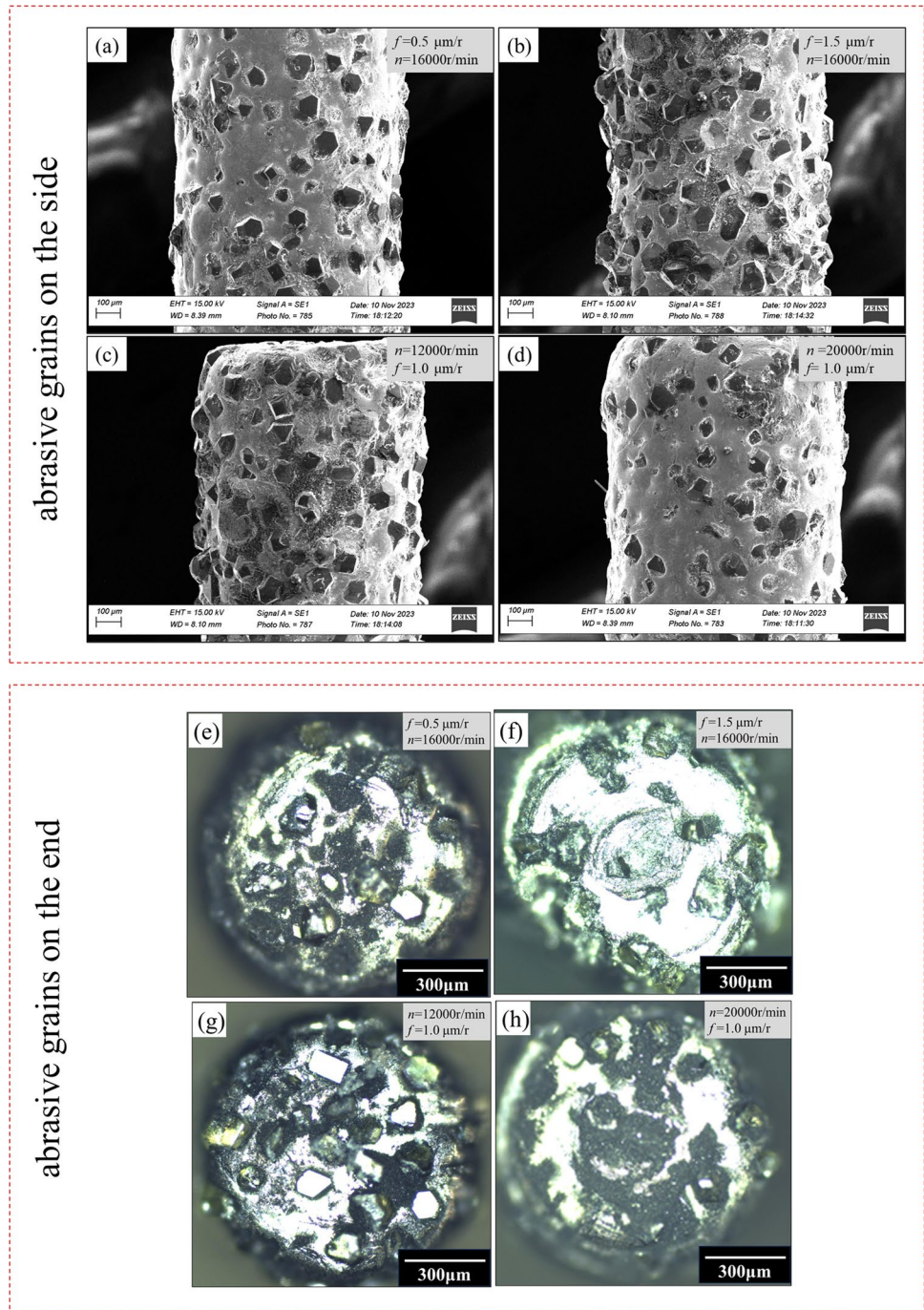
grains undergo significant wear. For example, the wear level is higher in Fig. 17(d) than in Fig. 17(c), and higher in Fig. 17(g) than in Fig. 17(h). The frequency at which a single abrasive grain sharpens the C_f/SiCs in a unit of time rises when n increases, resulting in increased abrasive grain wear. Additionally, the heat generated by the friction between the abrasive grains and the C_f/SiCs increases as n increases. This high temperature wears down the abrasive grains, further increasing the wear. In addition, it was found that the wear of the abrasive grains at the end of the grinding tool was more pronounced than on the grains on the sidewalls. The main reason is that the end of the abrasive grains mainly assists in material removal, and the chips produced at the end are not easy to discharge. Consequently, the end grains face more significant grinding force and heat, resulting in more severe wear. In contrast, sidewall grains mainly play a role in repairing the hole wall, and chips can be discharged from the spaces between the grains, leading to less wear.

4 Conclusion

This study investigates the grinding force, hole quality, and tool wear mechanism when machining 1 mm diameter holes in C/SiC composites using a brazed diamond grinding rod. The following conclusions were drawn:

(1) The grinding forces F_x, F_y, and F_z decrease with an increase in spindle speed and increase with an increase in feed rate. In addition, the thrust force F_z is greater than the radial forces F_x and F_y.

(2) Tear, burr, and chipping are the main defects observed at the entrance and exit of the hole surface. The damage factor, serving as the evaluation index for surface damage, is higher at the exit than at the entrance. This factor decreases with an increase in spindle speed and increases with an increase in feed rate. The diameter of the hole entrance exceeds 1000 μm due to the radial runout of the micro-grinding tool. The entrance diameter is larger than that of the exit, with a diameter error of less than 10%.

(3) The hole wall defects predominantly consist of carbon fiber fracture, carbon fiber pull-out, and spalling of SiC. The S_a gradually decreases with an increase in n. With an increase in f, S_a decreases and then increases. The hole wall morphologies vary with FOAs at 0°, 0–90°, 90°, and 90–180°, where the surface quality is poorest at an FOA of 90–180°.

(4) The wear on grains at the end of the grinding tool is more severe than on the side. Abrasive wear and diamond grain spalling are the main wear mechanisms. As the tool wears, the percentage of C elements on the tool surface decreases, while the percentages of Si and Ni

elements increase. Moreover, the wear of the abrasive grains increases with an increase in n and decreases with an increase in f.

This article has limited research on the material removal mechanism during the grinding process. Future studies will systematically investigate the material removal mechanism using nano-scratch tests.

Declarations

Conflict of interests The authors declare that they have no known competing financial interests or personal relationships that could have appeared to influence the work reported in this paper.

References

1. Wang XL, Gao XD, Zhang ZH, Cheng LS, Ma HP, Yang WM (2021) Advances in modifications and high-temperature applications of silicon carbide ceramic matrix composites in aerospace: A focused review. J Eur Ceram Soc 41:4671–4688. https://doi.org/10.1016/j.jeurceramsoc.2021.03.051

2. Ma XH, Zhao LF, Zhang Y, Li XQ, Cheng LF (2023) Uncertainty analysis and B-basis value of tensile strength of 2D SiC/SiC composite. J Mater Res Technol 24:7058–7067. https://doi.org/10.1016/j.jmrt.2023.04.253

3. Chen Z, Fang GD, Xie JB, Liang J (2016) Experimental study of high-temperature tensile mechanical properties of 3D needled C/C–SiC composites. Mater Sci Eng A 654:271–277. https://doi.org/10.1016/j.msea.2015.12.010

4. Diao QW, Zou HB, Ren XY, Wang CS, Wang Y, Li HY, Sui TY, Lin B, Yan S (2023) A focused review on the tribological behavior of C/SiC composites: Present status and future prospects. J Eur Ceram Soc 43:3875–3904. https://doi.org/10.1016/j.jeurceramsoc.2023.03.002

5. Krishnan SV, Ambalam MM, Venkatesan R, Mayandi J, Venkatachaleapathy V (2021) Technical review: Improvement of mechanical properties and suitability towards armor applications – Alumina composites. Ceram Int 47:23693–23701. https://doi.org/10.1016/j.ceramint.2021.05.146

6. Zhao GL, Zhao B, Ding WF, Xin LJ, Nian ZW, Peng JH, He N, Xu JH (2024) Nontraditional energy-assisted mechanical machining of difficult-to-cut materials and components in the aerospace community: a comparative analysis. Int J Extreme Manuf 6(2):022007. https://doi.org/10.1088/2631-7990/ad16d6

7. Zhang XH, Wang X, Jiao WL, Liu YT, Yu JY, Ding B (2023) Evolution from microfibers to nanofibers toward next-generation ceramic matrix composites: A review. J Eur Ceram Soc 43:1255–1269. https://doi.org/10.1016/j.jeurceramsoc.2022.11.033

8. Bingrui. L, B. Lin, T. Sui, C Liu, J Zhang, L Wang, X Chen, J Zhou (2023) Vibration-assisted material damage mechanism: From indentation cracks to scratch cracks. Chin J Aeronaut. https://doi.org/10.1016/j.cja.2023.12.013

9. Xue F, Zheng K, Liao WH, Shu J, Miao DD (2021) Experimental investigation on fatigue property at room temperature of C/SiC composites machined by rotary ultrasonic milling. J Eur Ceram Soc 41:3341–3356. https://doi.org/10.1016/j.jeurceramsoc.2021.01.046

10. Zhao GL, Nian ZW, Zhang ZH, Li L, He N (2023) Enhancing the machinability of Cf/SiC composite with the assistance of laser-induced oxidation during milling. J Mater Res Technol 22:1651–1663. https://doi.org/10.1016/j.jmrt.2022.12.050

11. Sharma A, Sharma N, Singh RP, Arora R, Gill RS, Singh G (2022) Micro-drill on Al/SiC composite by EDD process: An RSM-MOGOA based hybrid approach. Int J Lightweight Mater Manuf 5:564–575. https://doi.org/10.1016/j.ijlmm.2022.07.002

12. Zhang X, Yu T, Li M, Wang Z (2020) Effect of machining parameters on the milling process of 2.5 DC/SiC ceramic matrix composites. Mach Sci Technol 24:227–244. https://doi.org/10.1080/10910344.2019.1636271

13. Hu M, Ming WW, An QL, Chen M (2019) Experimental study on milling performance of 2D C/SiC composites using polycrystalline diamond tools. Ceram Int 45:10581–10588. https://doi.org/10.1016/j.ceramint.2019.02.124

14. Rösiger A, Goller R, Langhof N, Krenkel W (2021) Influence of in-plane and out-of-plane machining on the surface topography, the removal mechanism and the flexural strength of 2D C/C-SiC composites. J Eur Ceram Soc 41:3108–3119. https://doi.org/10.1016/j.jeurceramsoc.2020.10.063

15. Cao C, Song QH, Fu H, Ji HS, Liu ZQ, Jiang L (2023) Fiber orientation effects on grinding characteristics and removal mechanism of 2.5D Cf/SiC composites. Chinese J. Aeronaut. https://doi.org/10.1016/j.cja.2023.02.023.

16. Yan S, Diao QW, Chen BS, Zou HB, Ren XY, Wang Y, Zhang C, Sui TY, Lin B et al (2024) Nanosecond laser ablation behavior of C/SiC composites under water layer protection: Experiments and theoretical investigation. Opt Laser Technol 172:110516. https://doi.org/10.1016/j.optlastec.2023.110516

17. Jiao H, Chen B, Wang J, Su F (2023) Ablation of definite-depth blind holes in 2.5-dimensional C/SiC composites by nanosecond laser. J Manuf Process 91:78–88. https://doi.org/10.1016/j.jmapro.2023.02.020

18. Zhang YF, Liu D, Zhang WJ, Zhu HT, Huang CZ (2022) Hole characteristics and surface damage formation mechanisms of Cf/SiC composites machined by abrasive waterjet. Ceram Int 48:5488–5498. https://doi.org/10.1016/j.ceramint.2021.11.093

19. Zheng QZ, Mei XS, Jiang GD, Cui JL, Fan ZJ, Wang WJ, Yan ZX, Guo H, Pan AF (2023) Investigation on ultrasonic vibration-assisted femtosecond laser polishing of C/SiC composites. J Eur Ceram Soc 43:4656–4672. https://doi.org/10.1016/j.jeurceramsoc.2023.03.043

20. Hu YB, Cong WL (2018) A review on laser deposition-additive manufacturing of ceramics and ceramic reinforced metal matrix composites. Ceram Int 44:20599–20612. https://doi.org/10.1016/j.ceramint.2018.08.083

21. Natarajan Y, Murugesan PK, Mohan M, Khan SALA (2020) Abrasive Water Jet Machining process: A state of art of review. J Manuf, Process 49:271–322. https://doi.org/10.1016/j.jmapro.2019.11.030

22. Yang HT, Zhao GL, Nian ZW, Xin LJ, Li L (2023) Investigation of in-plane and out-of-plane micro-hole drilling on 2D-Cf/SiC composites. Ceram Int. https://doi.org/10.1016/j.ceramint.2023.12.391

23. Yang HT, Zhao GL, Nian ZW, Xin LJ, Li L, He N (2024) Effect of PCD tool wear on surface morphology and material removal mechanisms in the micro-drilling of Cf/SiC composites: Experiment and simulation. Int J Refract Met H 119:106562. https://doi.org/10.1016/j.ijrmhm.2024.106562

24. Zhang BY, Sui TY, Lin B, Zheng W, Li SP, Fang S, Huang Y, Feng YQ (2022) Drilling process of Cf/SiC ceramic matrix composites: Cutting force modeling, machining quality and PCD tool wear analysis. J Mater Process Technol 304:117566. https://doi.org/10.1016/j.jmatprotec.2022.117566

25. Li MJ, Jiang XY, Chen YJ, Yang XJ (2023) Hole surface morphology and tool wear mechanisms during cutting 3D carbon/carbon composites using diamond core drill. Ceram Int 49:6378–6388. https://doi.org/10.1016/j.ceramint.2022.10.128

26. Li MJ, Chen YJ, Tan MB, Yang XJ, Xiao Z (2023) Surface integrity and acoustic emission characteristics during slot milling 3D carbon/carbon composites using superabrasive diamond grinding point. Diam Relat Mater 137:110166. https://doi.org/10.1016/j.diamond.2023.110166

27. Chen B, Xu H, Guo Y, Guo B, Liu GY (2023) Experimental research on wear mechanism of diamond wheels for grinding Cf/SiC composites grooves. J Mater Res Technol 27:2382–2398. https://doi.org/10.1016/j.jmrt.2023.10.085

28. Huang XY, Jiang F, Wang ZB, Wu X, Huang SZ, Liu YF, Zhang JX, Shi XX (2023) A review on the balancing design of micro drills. Int J Adv Manuf Technol 131:4849–4871. https://doi.org/10.1007/s00170-023-11496-w